# Cryo-EM structures and binding of mouse ACE2 to SARS-CoV-2 variants of concern

Dongchun Ni[1], Priscilla Turelli[2], Bertrand Beckert[3], Sergey Nazarov[3], Emiko Uchikawa[3], Alexander Myasnikov[3], Florence Pojer[4], Didier Trono[2], Henning Stahlberg[1, $], Kelvin Lau[4,$]

[1] Laboratory of Biological Electron Microscopy (LBEM), Institute of Physics, School of Basic 15 Science, École Polytechnique Fédérale de Lausanne (EPFL), and Dep. of Fund. Microbiology, Faculty of Biology and Medicine, University of Lausanne, Lausanne, Switzerland

[2] Laboratory of Virology and Genetics (LVG), School of Life Sciences, École polytechnique fédérale de Lausanne (EPFL), Lausanne, Switzerland

[3]Dubochet Center for Imaging (DCI), École polytechnique fédérale de Lausanne (EPFL) and University of Lausanne, Lausanne, Switzerland

[4]Protein Production and Structure Characterization Core Facility (PTPSP), School of Life Sciences, École polytechnique fédérale de Lausanne (EPFL), Lausanne, Switzerland

[$] Corresponding authors: henning.stahlberg@epfl.ch, kelvin.lau@epfl.ch

## ABSTRACT

Investigation of potential hosts of the severe acute respiratory syndrome coronavirus-2 (SARS-CoV-2) is crucial to understanding future risks of spillover and spillback. SARS-CoV-2 has been reported to be transmitted from humans to various animals after requiring relatively few mutations.[1] Mice are well adapted to human environments, frequently come in contact with humans, are used widely as infection models, and may act as reservoirs for SARS-CoV-2.[2] Structural and binding data of the mouse ACE2 receptor with the Spike protein of newly identified SARS-CoV-2 variants are needed to better understand the impact of variants of concern (VOC). Previous studies have developed mouse-adapted variants and have identified some determinants of binding.[3,4] Here we report the cryo-EM structures of mouse ACE2 bound to Spike ectodomains of four different VOC: Beta, Omicron BA.1, Omicron BA.2.12.1 and Omicron BA.4/5. These variants represent the oldest to the newest variants that are able to bind the mouse ACE2 receptor. Our high-resolution structural data

complemented with bio-layer interferometry (BLI) binding assays reveal a requirement for a combination of mutations in the Spike protein to enable the binding to mouse ACE2.

We performed BLI binding assays between SARS-CoV2 variants of concern to characterize the binding affinities of dimeric mouse ACE2 (mACE2) compared to that of the human receptor (hACE2). The wild-type Spike protein bound robustly hACE2 but not strongly to mACE2, with only appreciable signal at the highest concentration of 300 nM (Supplementary information, Fig. S1). With the emergence of the first generation of SARS-CoV2 variants, Alpha, Beta and Gamma, all sharing the N501Y mutation in their Spike protein (Supplementary information, Fig. S2), it was reported that mice were susceptible to infection.[5–7] We observed an increase in affinity to the mACE2 where we could detect appreciable binding with dissociation constants ($K_d$) measuring below 100 nM as compared to wild-type (Fig. 1a, Supplementary information, Fig. S1). mACE2 increased its affinity for Spike further with the appearance with Omicron BA.1 and BA.2 with up to 10-fold increase compared to wild-type (Fig. 1a, Supplementary information, Fig. S1). The Spike protein from more recent Omicron BA.2.12.1 and BA.4/5 variants, containing additional mutations, still bound strongly to the receptor binding domain (RBD) interface (Fig. 1a, Supplementary information, Fig. S2). To probe how variants of concern gained high affinity mACE2 binding, utilizing cryo-EM, we determined the structures of four mACE2/Spike VOC complexes spanning the variants Beta, Omicron BA.1, BA.2.12.1, and BA.4/5, at resolutions of 3.9 Å, 2.7Å, 2.9 Å and 2.9Å, respectively (Fig. 1b and Supplementary information, Figs. S3-S7). We also solved the hACE2/BA.4/5 Spike complex at 2.8Å for comparison (Supplementary information, Fig. S7). All of the structures show that mACE2/hACE2 bind the RBD of the Spike protein in the same manner at the binding ridge of a RBD in the up-position. During cryo-EM data-processing we observed the RBD of all Spikes in either a 2-up or 3-up conformation, with each up-RBD having an ACE2 bound (Supplementary information, Figs. S3-S7). To gain structural information at side-chain level resolution of the binding interface, we performed image processing of the cryo-EM data by location-focused refinement. This yielded maps at higher quality for each variant's ACE2/RBD interface, allowing to better understand the effects of mutations in these regions (Fig. 1c, Supplementary information, Figs. S3-S8).

SARS-CoV2 variants Alpha, Beta and Gamma the first reported to be able to engage mACE2, and all share a crucial N501Y mutation in their Spike proteins. In the mACE2/Beta

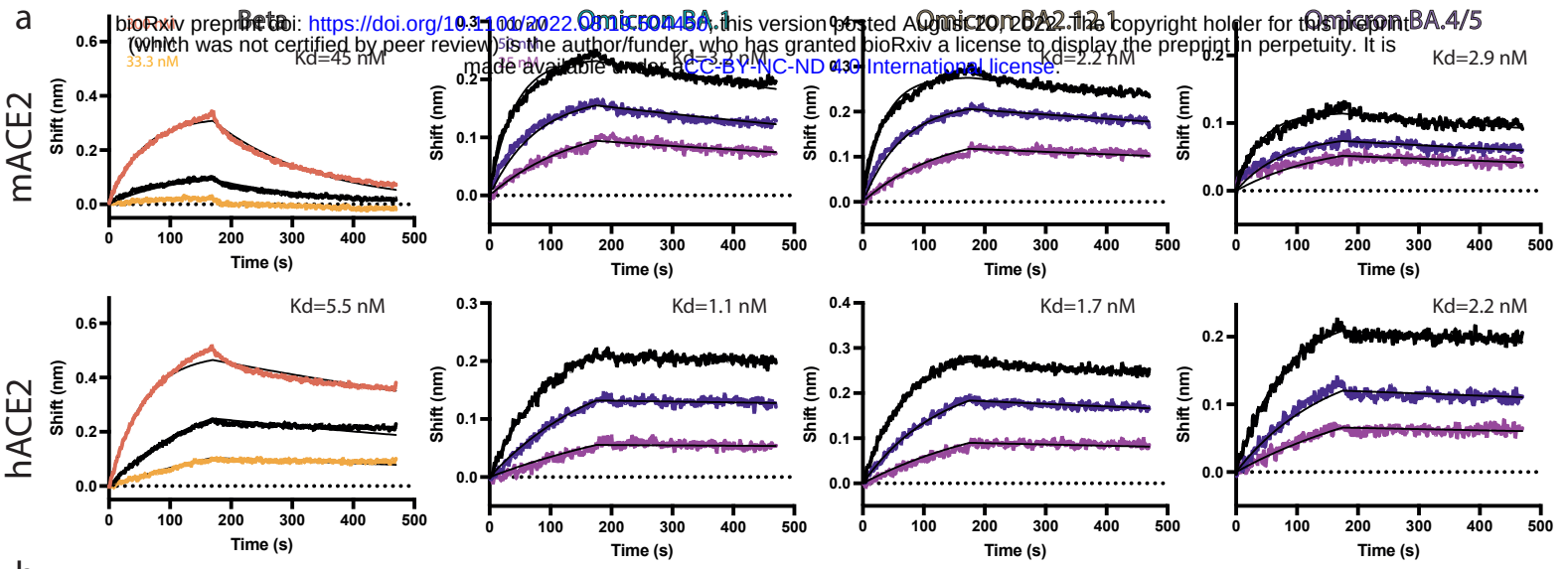


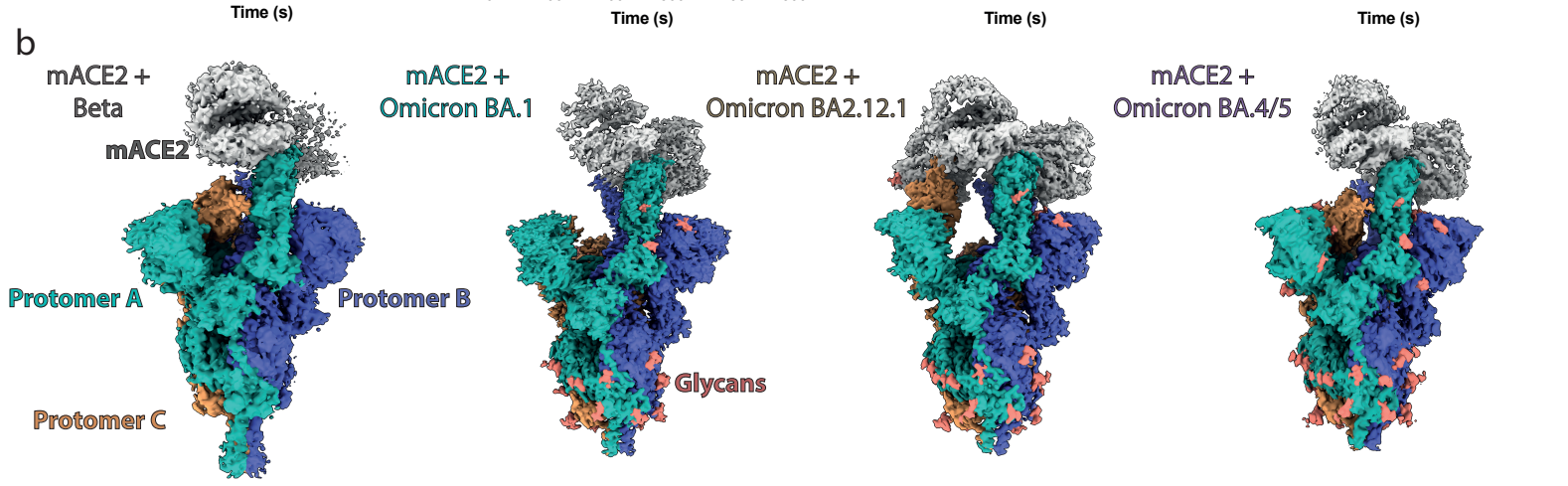


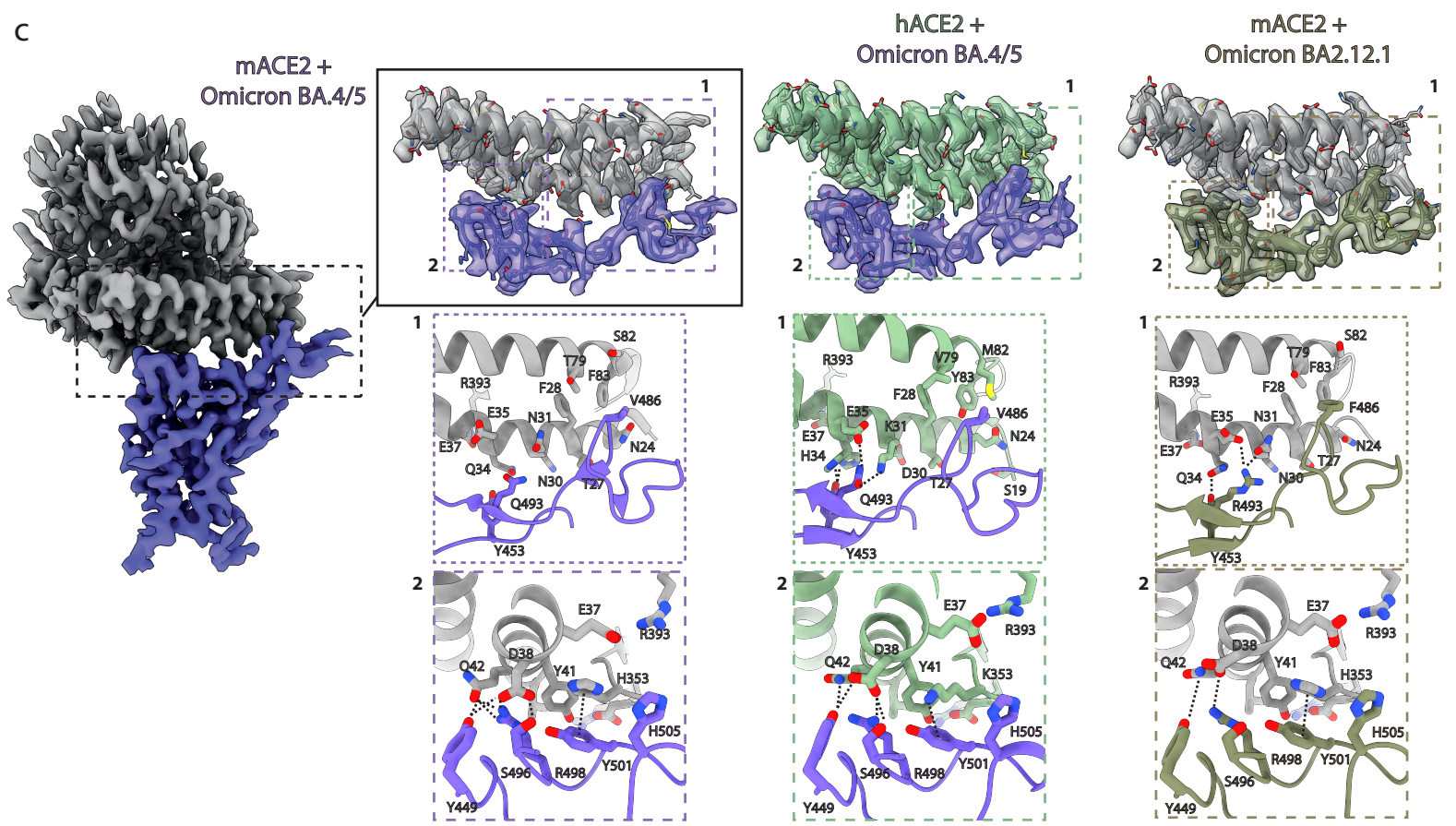


d

| | 19 | 24 | 27 | 28 | 30 | 31 | 34 | 35 | 37 | 38 | 41 | 42 | 45 | 79 | 82 | 83 | 330 | 353 | 355 | 357 | 393 |
|---|---|---|---|---|---|---|---|---|---|---|---|---|---|---|---|---|---|---|---|---|---|
| human | S | Q | T | F | D | K | H | E | E | D | Y | Q | L | L | M | Y | N | K | D | R | R |
| mouse | S | N | T | F | N | N | Q | E | E | D | Y | Q | L | T | S | F | N | H | D | R | R |
| hamster | S | Q | T | F | D | K | Q | E | E | D | Y | Q | L | L | N | Y | N | K | D | R | R |
| cat | S | L | T | F | E | K | H | E | E | E | Y | Q | L | L | T | Y | N | K | D | R | R |
| dog | - | L | T | F | E | K | Y | E | E | E | Y | Q | L | L | T | Y | N | K | D | R | R |
| mink | S | L | T | F | E | K | Y | E | E | E | Y | Q | L | H | T | Y | N | K | D | R | R |

**Figure 1**

structure, we observe that the Spike N501Y mutation, which replaces a polar asparagine (N) residue with a polar and aromatic tyrosine (Y) residue, allows for π-π interactions with Y43 of mACE2, and potentially enables a new cation-π and hydrogen bond interaction with the histidine H353, which is unique to the mouse mACE2 (Supplementary information, Fig. S9). This crucial Spike Y501 is also present in all later identified Omicron Spike variants. Beta and Gamma also share E484K and K417N/T as signature mutations in the Spike's RBD (Supplementary information, Fig S2). These two residues are unfortunately not resolved in our cryo-EM maps. However, *in vitro* BLI experiments showed that alongside N501Y, the E484K mutation can confer high-affinity binding of the Spike to mACE2 (Supplementary information, Fig. S1). We could not observe any binding of single mutants of N501Y, E484K or K417N of the Spike protein to mACE2. Only the combined presence of Y501 and K484 in the Spike protein showed binding to mACE2 at the concentration of Spike protein tested here (75 nM).

We next investigated Omicron variants BA.1, BA.2, BA.2.12.1 and BA.4/5 that most recently caused new waves of infections in several countries during the year 2022.[8,9] These variants contain up to 34 mutations scattered across the entire Spike protein, with the majority concentrated on the RBD, including N501Y and E484A (Supplementary information, Fig. S2). The accumulation of these mutations prompted an ongoing discussion about a possible murine origin of the Omicron variant.[10] Indeed, our here presented mACE2/BA.1 structure reveals multiple new interactions localized in two different patches. In patch 1, the longer arginine (R) sidechain of the BA.1 RBD Q493R mutation allows for hydrogen bonding with mACE2 residues N31 and Q34, which was not possible with the shorter glutamine (Q) residue present in the original Spike protein (Supplementary information, Fig. S9). In patch 2, Y501 is observed to form cation-π interactions with H353 from mACE2, and new BA.1 mutations G496S and Q498R form a new set of hydrogen-bonds and electrostatic interactions with mACE2's aspartic acid D38 (Supplementary information, Fig. S9). Overall, Omicron BA.1 mutations Q493R and Q498R are crucial for stronger binding to mACE2, alongside with the N501Y and E484A/K mutations present in preceding variants. These new interactions greatly increase the binding between mACE2 and Omicron Spike proteins with measured affinities by BLI up to 14-20-fold stronger compared to Beta (Fig. 1 and Supplementary information, Fig. S1).

Both the BA.2.12.1 and BA.4/5 Omicron subvariants carry the immune-evading L452R mutation first seen in the Delta variant. The site of mutation is not within the RBD-ACE2 binding interface and, as expected, the binding affinities for both hACE2 and mACE2 binding to BA.2.12.1 are unchanged compared to BA.2 (Fig. 1a, Supplementary information, Fig. S1). In the mACE2/BA.2.12.1 structure, the critical interactions made by Spike residues R498 and Y501 with mACE2 within patch 2 are conserved as in BA.1 (Fig. 1c). Interestingly, R493 of BA.2.12.1 has an alternative hydrogen bonding network with N31 and E35, instead of Q34, which now forms a hydrogen bond with Y453 of mACE2 suggesting a plasticity in its interactions (Fig. 1c).

The Omicron subvariants BA.4 and BA.5 that were the principal variants during an infection wave in the summer of 2022, share the L452R mutation. In addition, BA.4 and BA.5 contain the F486V mutation, and the reversion of R493 back to the wild-type Q493 (Supplementary information, Fig. S2). The structure the mACE2/BA.4/5 complex show crucial changes at patch 1, where the BA.4/5 mutation F486V loses Van der Waals interactions with adjacent mACE2 residues F83 and F28, and the wild-type Q493 (R493Q wild-type reversion) on the Spike's RBD no longer forms interactions with mACE2 (Fig. 1c). The hACE2/BA.4/5 structures reveal the same loss of interactions for the Spike's F486V mutation, but the Spike's Q498 once again allows for an interaction to be formed with hACE2's K31, which was not possible with the Spike's R498 due to its charge repulsion from hACE's K31 (Fig. 1c). The two mutations together allow for BA.4/5 Spike to maintain high affinity interactions with both, hACE2 and mACE2. This is an example of the interplay between balancing immune evasion, while maintaining high-affinity receptor binding. The other principal interactions between mACE2 and Spike's BA.4/5 in patch 2 are comparable to those observed between mACE2 and variants BA.1 or BA2.12.1.

In summary, our structural data and binding analysis of mACE2 to SARS-CoV-2 variants of concern highlight the evolutionary adaptations that have allowed the virus to evade the human immune system, and how those mutations impacted receptor binding in mice. Our results identified critical mutations of SARS-CoV-2's Spike protein, N501Y, E484K, Q493R and Q498R, that are required for high-affinity binding to mACE2, contributing a structural basis for our understanding of the potential of spillback of SARS-CoV-2 into the animal kingdom.

## FIGURE LEGENDS

**Fig. 1**: Structural basis for mACE2 binding to Omicron variants of concern. **a** BLI binding assays of captured dimeric mouse or human ACE2 versus various concentrations of Spike variants of concern. Data curves are colored by concentration and the black line indicates the 1:1 fit of the data. **b** Cryo-EM densities of the full mACE2/Spike variant of concern complexes. Each protomer of the Spike trimer is colored separately with mACE2 colored in grey. **c** Focused refinement of the RBD-ACE2 interface of the mACE2 BA.4/5 complex showing the cryo-EM density. Inset shows the zoomed view of the binding interface. The same view is shown for the hACE2/BA.4/5 and mACE2/BA2.12.1 complexes. **d** Zoomed views of specific interaction sites of patch 1 and patch 2 as indicated in (**c**). **e** Sequence alignment of human ACE2 with mouse ACE2 and other selected species. Red boxes highlight critical differences between human and mouse ACE2 residues.

## DATA AVAILABILITY

Cryo-EM maps for the Spike variants in complex with mouse ACE2 were deposited in the Electron Microscopy Data Bank (EMDB) under the access codes EMD-15541 (full map, Beta, two mACE2 bound), EMD-15589 (local map, mACE2/Beta), EMD- 15580 (full map, BA.1, two mACE2 bound), EMD-15581 (full map, BA.1, three mACE2 bound), EMD-15590 (local map, mACE2/BA.1), EMD-15584 (full map, BA.2.12.1, two mACE2 bound), EMD-15585 (full map, BA2.12.1, three mACE2 bound), EMD-15591 (local map, mACE2/BA.2.12.1), EMD-15586 (full map, BA.4/5, two mACE2 bound) and EMD-15592 (local map, mACE2/BA.4/5).

Maps for Spike the human ACE2/Omicron BA.4/5 complex were deposited in the EMDB under the access codes EMD-15587 (full map, BA.4/5, three hACE2 bound) and EMD-15588 (local map, hACE2/BA.4/5).

Atomic models were deposited in Protein Data Bank (PDB) under the access codes of PDB-8AQS (hACE2-BA.4/5), PDB-8AQT (mACE2/Beta), PDB-8AQU (mACE2/BA.1), PDB-8AQV (mACE2/BA.2.12.1) and PDB-8AQW (mACE2/BA.4/5).

Raw electron microscopy image data were deposited at the Electron Microscopy Public Image Archive (EMPIAR) under access codes EMPIAR-XXXXX (Beta, two mACE2 bound), EMPIAR-XXXXX (BA.1, two mACE2 bound), EMPIAR-XXXXX (BA.1, three

mACE2 bound), EMPIAR-XXXXX (BA.2.12.1, two mACE2 bound), EMPIAR-XXXXX (BA2.12.1, three mACE2 bound), and EMPIAR-XXXXX (BA.4/5, two mACE2 bound).

## CONTRIBUTIONS

D.N., K.L., P.T., F.P., D.T. designed the project. P.T. designed and cloned the Spike variants. K.L purified the Omicron Spike and ACE2 and performed BLI assays. B.B., S.N., E.U., A.M., froze and screened cryo-EM grids, collected data, and performed on-the-fly processing. D.N. processed cryo-EM data and built models. D.N. and K.L. analyzed data and prepared figures. K.L., D.N., wrote the manuscript. F.P., H.S., and D.T. supervised the project.

## ACKNOWLEDGEMENTS

Cryo-EM data collection and initial image processing was performed at the Dubochet Center for Imaging, a common initiative of the EPFL, UNIL and UNIGE, with data collection performed in both Geneva and Lausanne. We thank Yashar Sadian for data collection on the Talos Arctica. We thank Rosa Schier, Laurence Durrer, Soraya Quinche and Michael François of the Protein Production and Structure Core Facility of EPFL for helping in the production of Spike Omicron and ACE2. Charlene Raclot for cloning of the Spike variants. This work was supported in part by NCCR TransCure, a National Centre of Competence in Research, funded by the Swiss National Science Foundation (grant number 185544)

## REFERENCES

1. Tan, C. C. S. *et al.* Transmission of SARS-CoV-2 from humans to animals and potential host adaptation. *Nat Commun* **13**, 2988 (2022).
2. Muñoz-Fontela, C. *et al.* Advances and gaps in SARS-CoV-2 infection models. *PLOS Pathogens* **18**, e1010161 (2022).
3. Sun, S. *et al.* Characterization and structural basis of a lethal mouse-adapted SARS-CoV-2. *Nat Commun* **12**, 5654 (2021).
4. Dinnon, K. H. *et al.* A mouse-adapted model of SARS-CoV-2 to test COVID-19 countermeasures. *Nature* **586**, 560–566 (2020).

5. Yao, W. *et al.* Circulating SARS-CoV-2 variants B.1.1.7, 501Y.V2, and P.1 have gained ability to utilize rat and mouse Ace2 and altered in vitro sensitivity to neutralizing antibodies and ACE2-Ig. *bioRxiv* 2021.01.27.428353 (2021) doi:10.1101/2021.01.27.428353.
6. Thakur, N. *et al.* SARS-CoV-2 variants of concern alpha, beta, gamma and delta have extended ACE2 receptor host ranges. *Journal of General Virology* **103**, 001735.
7. Montagutelli, X. *et al. The B1.351 and P.1 variants extend SARS-CoV-2 host range to mice*. http://biorxiv.org/lookup/doi/10.1101/2021.03.18.436013 (2021) doi:10.1101/2021.03.18.436013.
8. Viana, R. *et al. Rapid epidemic expansion of the SARS-CoV-2 Omicron variant in southern Africa*. 2021.12.19.21268028 https://www.medrxiv.org/content/10.1101/2021.12.19.21268028v1 (2021) doi:10.1101/2021.12.19.21268028.
9. Tegally, H. *et al.* Emergence of SARS-CoV-2 Omicron lineages BA.4 and BA.5 in South Africa. *Nat Med* 1–6 (2022) doi:10.1038/s41591-022-01911-2.
10. Wei, C. *et al.* Evidence for a mouse origin of the SARS-CoV-2 Omicron variant. *Journal of Genetics and Genomics* (2021) doi:10.1016/j.jgg.2021.12.003.
11. Punjani, A., Rubinstein, J. L., Fleet, D. J. & Brubaker, M. A. cryoSPARC: algorithms for rapid unsupervised cryo-EM structure determination. *Nat Methods* **14**, 290–296 (2017).
12. Pettersen, E. F. *et al.* UCSF Chimera—A visualization system for exploratory research and analysis. *Journal of Computational Chemistry* **25**, 1605–1612 (2004).
13. Emsley, P., Lohkamp, B., Scott, W. G. & Cowtan, K. Features and development of Coot. *Acta Cryst D* **66**, 486–501 (2010).
14. Liebschner, D. *et al.* Macromolecular structure determination using X-rays, neutrons and electrons: recent developments in Phenix. *Acta Cryst D* **75**, 861–877 (2019).

15. Pettersen, E. F. *et al.* UCSF ChimeraX: Structure visualization for researchers, educators, and developers. *Protein Science* **30**, 70–82 (2021).

## Supplementary Information

## METHODS AND MATERIALS

### Protein Production and Purification

The Spike trimer was designed to mimic the native trimeric conformation of the protein in vivo and the expression vector was kindly provided by Prof. Jason McLellan, University of Texas, Austin (TX), USA. It encoded the prefusion ectodomain of the original 2019-CoV Spike, containing a native signal peptide, residues 986 and 987 mutated to proline (2P), a mutated putative furin cleavage site (residues 682-685 mutated to GSAS), a C-terminal T4 foldon fusion domain to stabilize the trimer complex, followed by C-terminal 8x His and 2x Strep tags for affinity purification. The trimeric Spike protein was transiently expressed in suspension-adapted ExpiCHO cells (Thermo Fisher) in ProCHO5 medium (Lonza) at 5 x$10^6$ cells/mL using PEI MAX (Polysciences) for DNA delivery. At 1 h post-transfection, dimethyl sulfoxide (DMSO; AppliChem) was added to 2% (v/v). Following a 7-day incubation with agitation at 31 °C and 4.5% $CO_2$, the cell culture medium was harvested and clarified using a 0.22 µm filter. The conditioned medium was loaded onto Streptactin XT columns (IBA) washed with PBS and eluted with 50 mM biotin in 150 mM NaCl, 100 mM HEPES 7.5. Eluted protein was then dialyzed overnight into PBS. The purity of Spike trimers was determined to be >99% pure by SDS-PAGE analysis. Point mutations were generated by InFusion-mediated site directed mutagenesis. Variant clones were generated by gene synthesis (Twist Biosciences, Genscript and IDT) on the 2019-CoV Spike background as above. All mutants were produced and purified in an identical manner to the original 2019-Cov S protein.

### Cryo-electron microscopy

### mACE2/Beta complex

Cryo-EM grids were prepared with a Leica EM GP2 (Leica) plunge-freezing device, using Quantifoil R2/1 copper 400 grids. 3.0 µL of a sample containing 0.4 µM Beta Spike and 0.7 µM mACE2-Fc was applied to the glow-discharged grids, and backblotted for 2 s with a 10 s

wait time, 80% humidity and 10 °C in the sample chamber, and the blotted grids were plunge-frozen in liquid nitrogen-cooled liquid ethane.

Grids were screened for particle presence and ice quality on a TFS Talos Arctica transmission electron microscope (TEM) operated at 200kV. Cryo-EM data was collected using the same microscope, equipped with a TFS Falcon 3 camera. Movies were recorded at a nominal magnification of 150kx, corresponding to a 0.9759Å pixel, with defocus values ranging from -0.8 to -2.5 µm. Exposures were adjusted automatically to 40 e-/Å2 total dose with automatic collection using EPU.

**mACE2/Omicron BA.1 complex**

Cryo-EM grids were prepared with a Vitrobot Mark IV (Thermofisher Scientific (TFS)). Quantifoil R1.2/1.3 Au 400 holey carbon grids were glow-discharged for 120 s at 15mA using a PELCO easiGlow device (Ted Pella, Inc.). 3.0 µL of a sample containing 9 µM Omicron BA.1 and 16 µM mACE-Fc was applied to the glow-discharged grids, and blotted for 6 s under blot force 10 at 100% humidity and 4 °C in the sample chamber, and the blotted grids were plunge-frozen in liquid nitrogen-cooled liquid ethane.

Grids were screened for particle presence and ice quality on a TFS Glacios TEM (200kV), and the best grids were transferred to TFS Titan Krios G4 TEM. Cryo-EM data was collected using TFS Titan Krios G4, equipped with a Cold-FEG and Selectris X energy filter, on a Falcon IV detector in electron counting mode. Falcon IV gain references were collected just before data collection. Data was collected using TFS EPU v2.12.1 using aberration-free image shift protocol (AFIS). Movies were recorded at the nominal magnification of 165kx, corresponding to the 0.726Å pixel size at the specimen level, with defocus values ranging from -0.7 to -2.0 µm. Exposures were adjusted automatically to 60 e-/Å$^2$ total dose.

**hACE2/Omicron BA.4/5, mACE2/Omicron BA.4/5, mACE2/Omicron BA.2.12.1**

Cryo-EM grids were prepared with a Vitrobot Mark IV (Thermofisher Scientific (TFS)). Quantifoil R1.2/1.3 Au 400 holey carbon grids were glow-discharged for 120 s at 15mA using a PELCO easiGlow device (Ted Pella, Inc.). 3.0 µL of a sample containing 14 µM of the corresponding Spike and 25 µM mACE-Fc was applied to the glow-discharged grids, and

blotted for 6 s under blot force 10 at 100% humidity and 4 °C in the sample chamber, and the blotted grid was plunge-frozen in liquid nitrogen-cooled liquid ethane.

Grids were screened for particle presence and ice quality on a TFS Glacios TEM (200kV), and the best grids were transferred to TFS Titan Krios G4 TEM. Cryo-EM data was collected using the TFS Titan Krios G4 TEM, equipped with a Cold-FEG, on a Falcon IV detector in electron counting mode. Falcon IV gain references were collected just before data collection. Data was collected using TFS EPU v2.12.1 using aberration-free image shift protocol (AFIS). Movies were recorded at nominal magnification of 165kx, corresponding to the 0.83Å pixel size at the specimen level, with defocus values ranging from -0.7 to -2.5 µm. Exposures were adjusted automatically to 60 e-/Å2 total dose.

**Cryo-EM image processing**

On-the-fly processing was first performed during data acquisition for evaluating the data quality during screening by using cryoSPARC live v3.3.1.4.[11] The obtained ab-initio structures were used as templates for better particle picking. Motion correction was performed on raw stacks without binning, using the cryoSPARC implementation of motion correction. The full data processing workflow is shown in Supplementary information, Figs. S3-S8 and processing statistics on Table 1.

**Cryo-electron microscopy model building**

The models of a SARS-CoV2 Spike (PDB ID 7QO7), mouse ACE2 (PDB ID 7FDK) and human ACE2 (PDB ID 7FDG) were re-fit into the cryo-EM maps with UCSF Chimera.[12] These docked models were extended and rebuilt manually with refinement, using Coot and Phenix.[13,14] Figures were prepared in UCSF ChimeraX.[15]

**Biolayer Interferometry (BLI)**

All experiments were performed on a Gator BLI system. Running buffer was 150 mM NaCl, 10 mM HEPES 7.5. For binding assays, dimeric Fc-ACE2 was diluted to 10 µg/mL and captured with MFc tips (GatorBio). Loaded tips were dipped into a 3 or 2-fold serial dilution series (300 nM, 100 nM, 33.3 nM, or 100 nM, 50 nM, 25 nM) of target analyte Spike protein. Screening of independent point mutations was done as above at a single concentration of 75 nM. Curves were processed using the Gator software with a 1:1 fit after background subtraction. Plots were generated in Prism 9.

a

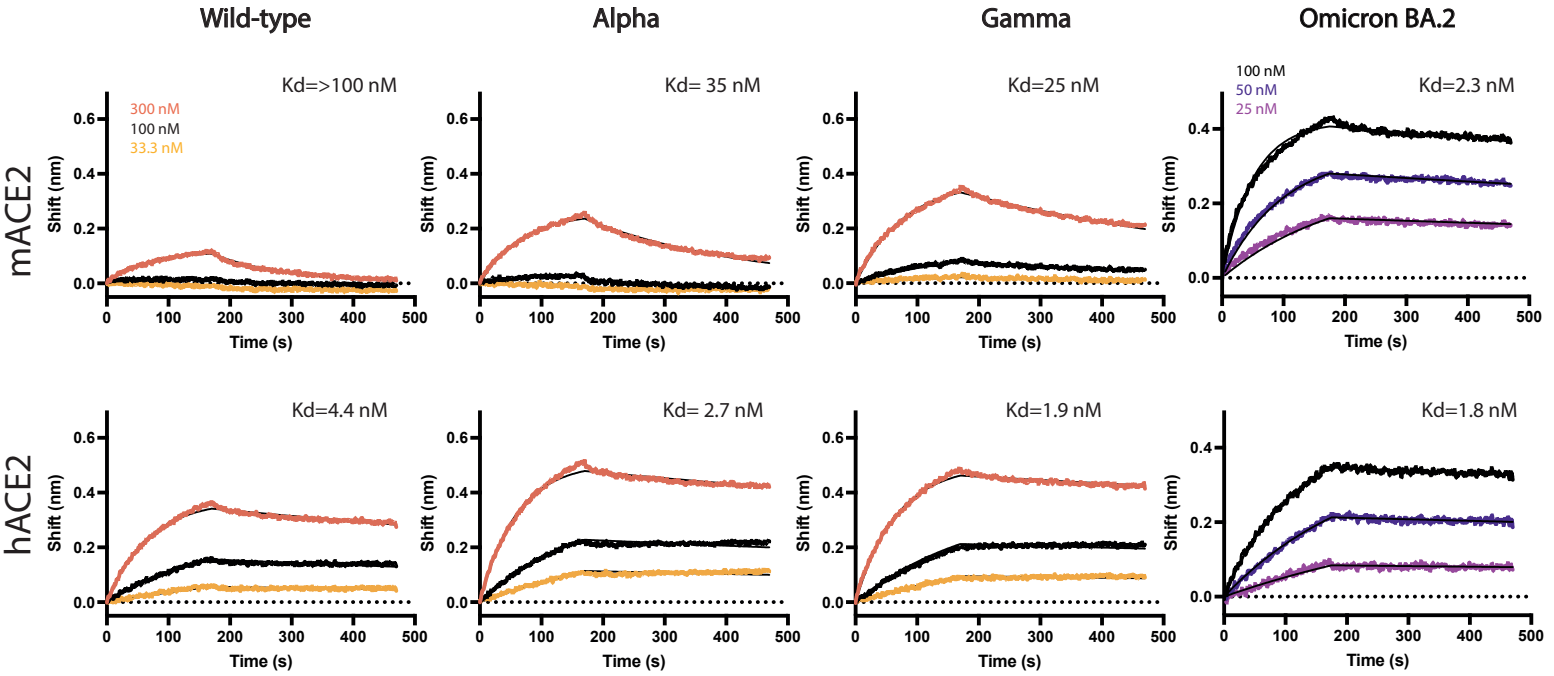


b

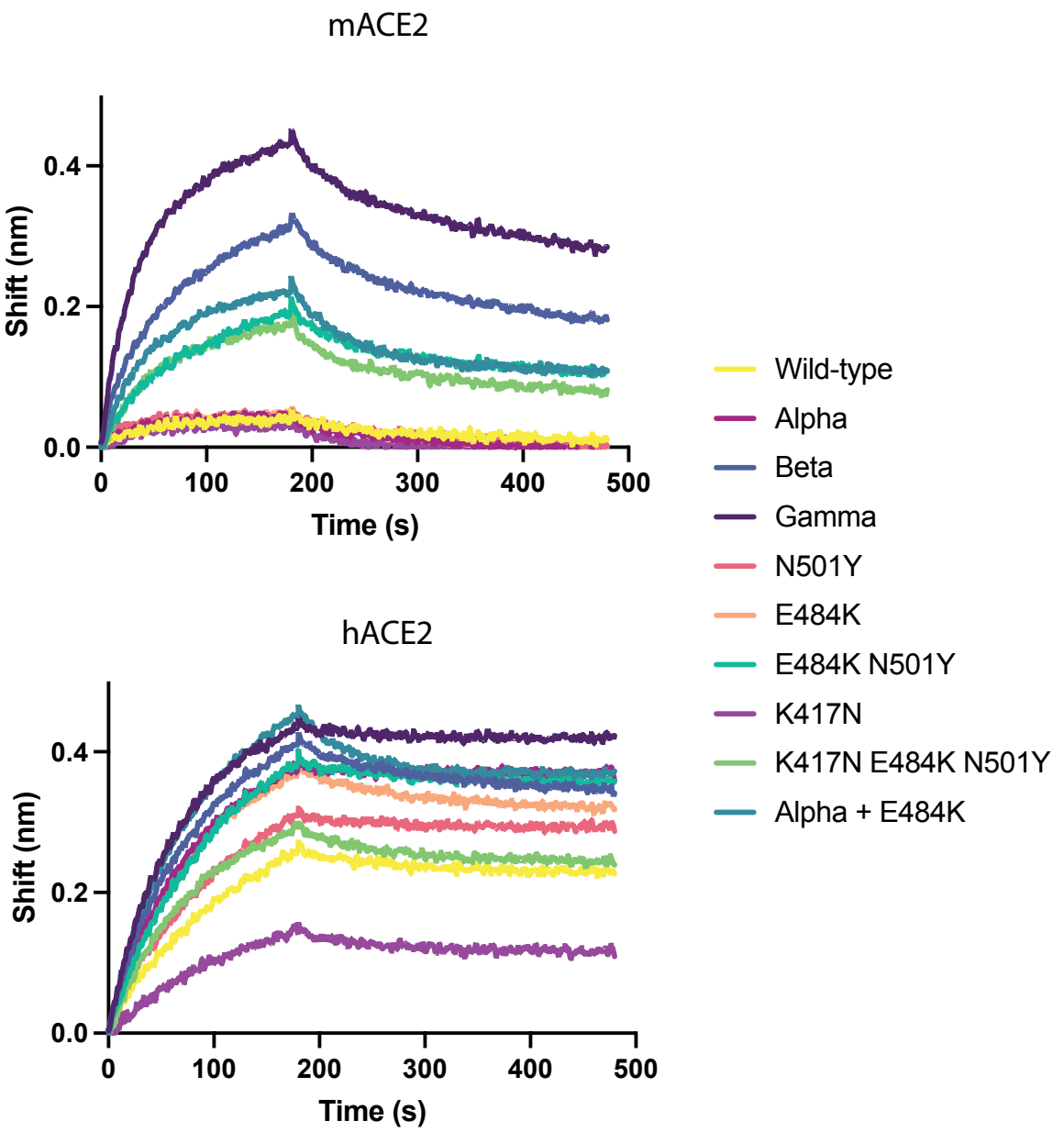


**Figure S1**

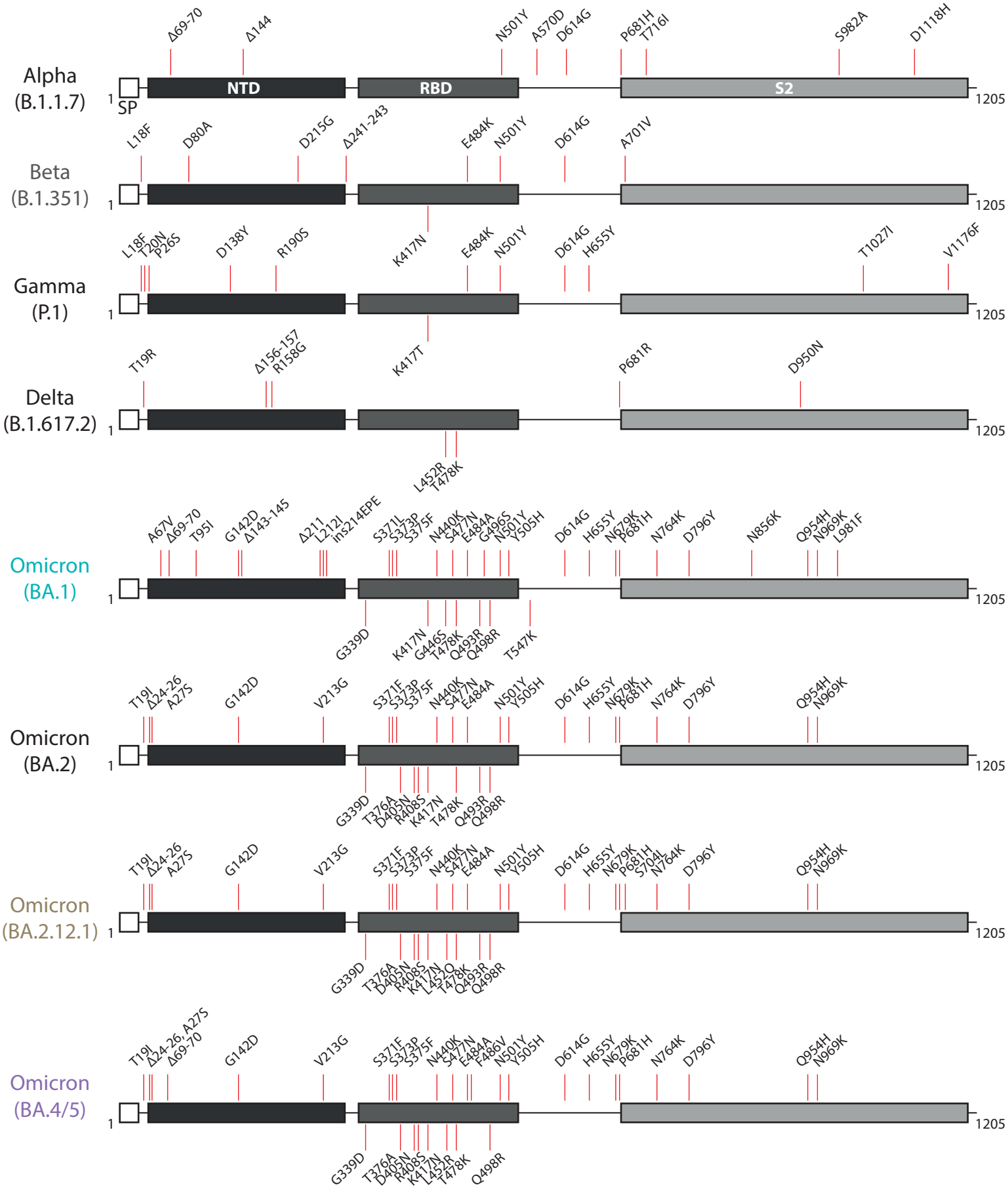


**Figure S2**

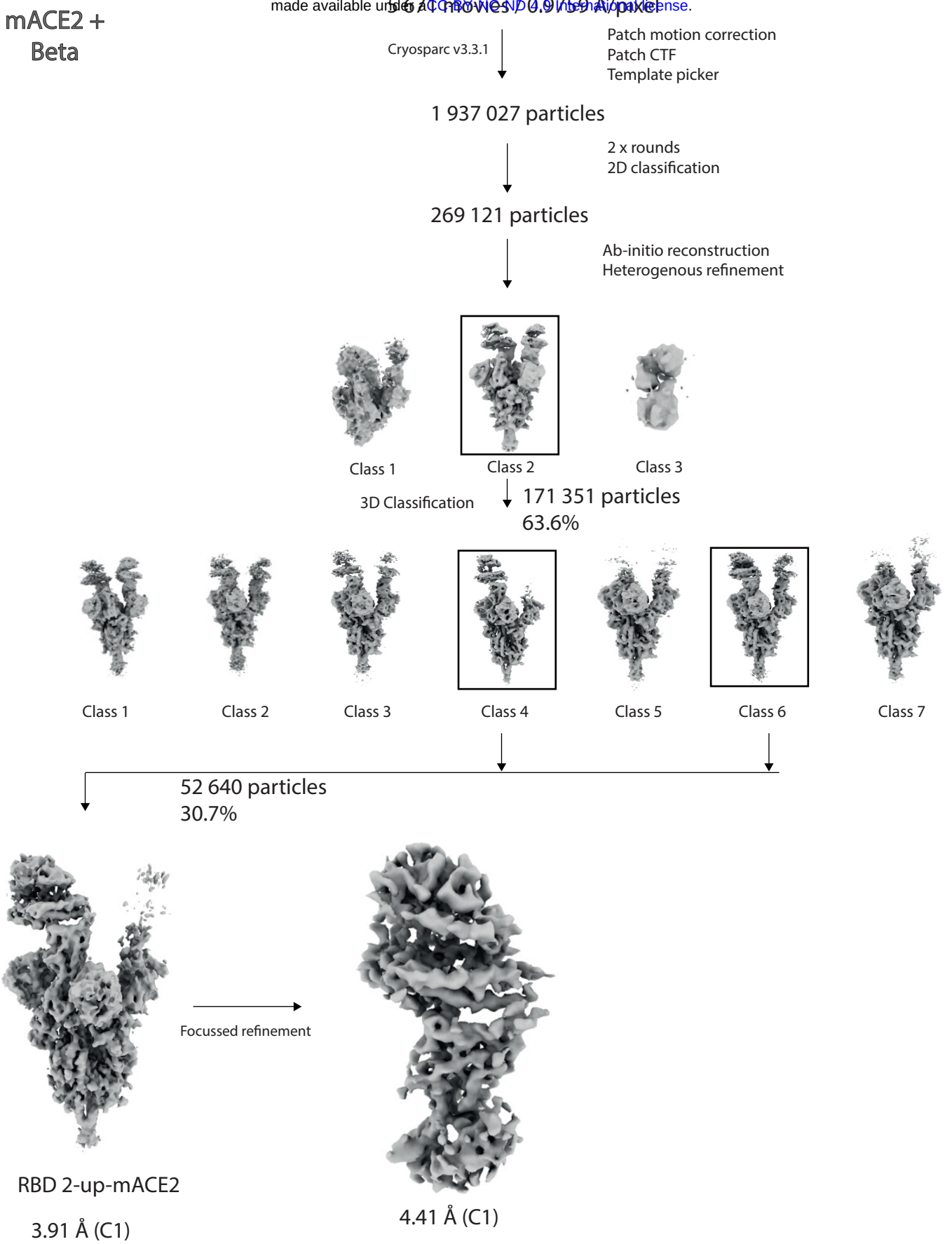


**Figure S3**

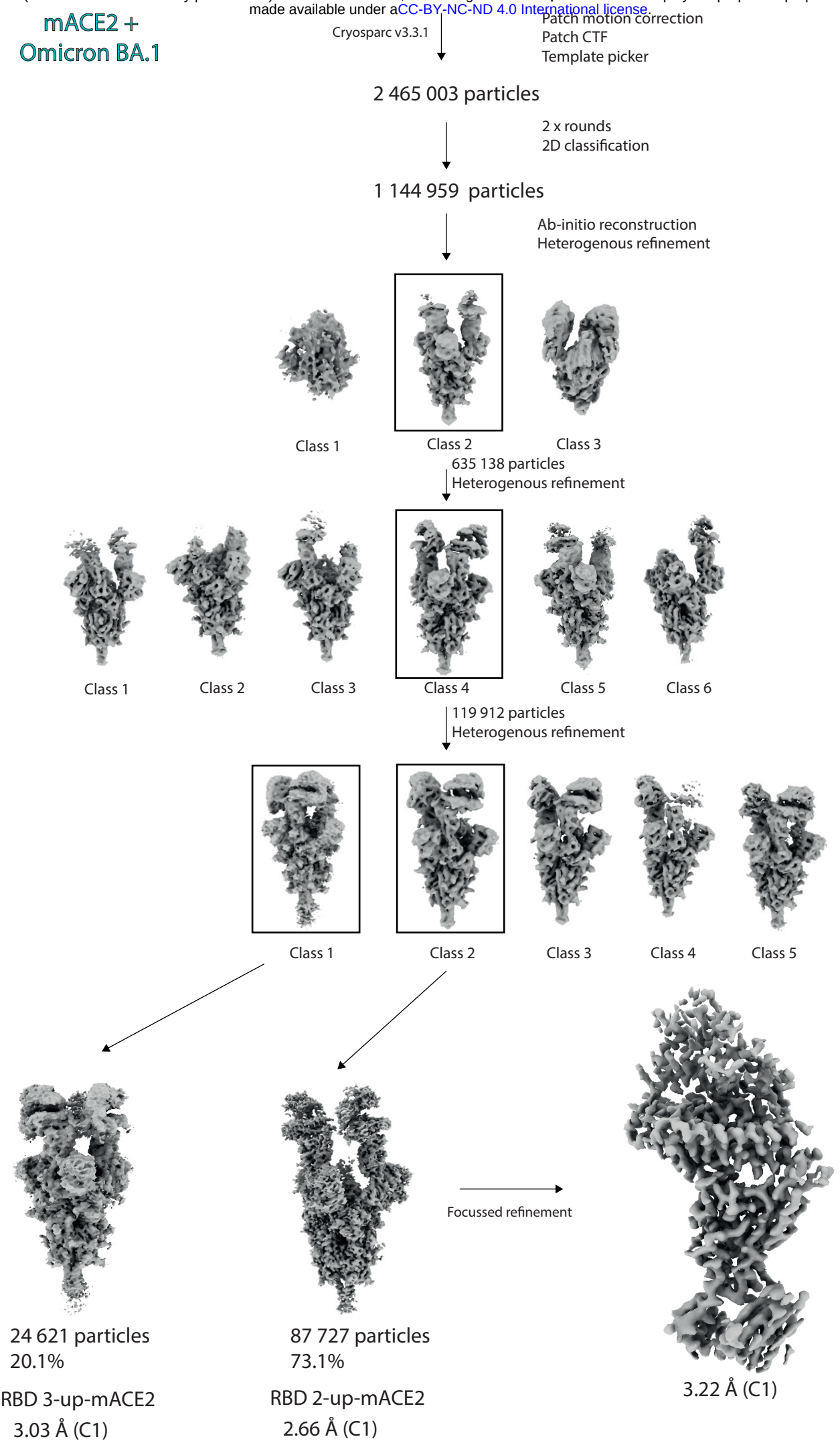


**Figure S4**

mACE2 + Omicron BA2.12.1

8 046 movies, 0.83 Å/pixel

Cryosparc v3.3.1

Patch motion correction
Patch CTF
Template picker

2 235 516 particles

3 x rounds
2D classification

878 099 particles

Ab-initio reconstruction
Heterogenous refinement

Class 1 | Class 2 | Class 3 | Class 4 | Class 5

629 601 particles
Heterogenous refinement

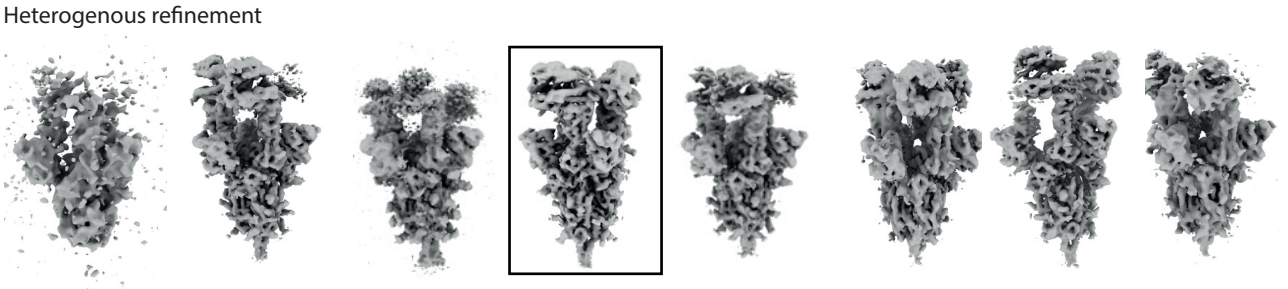

Class 1 | Class 2 | Class 3 | Class 4 | Class 5 | Class 6 | Class 7 | Class 8

208 626 particles, 33.1%
Heterogenous refinement

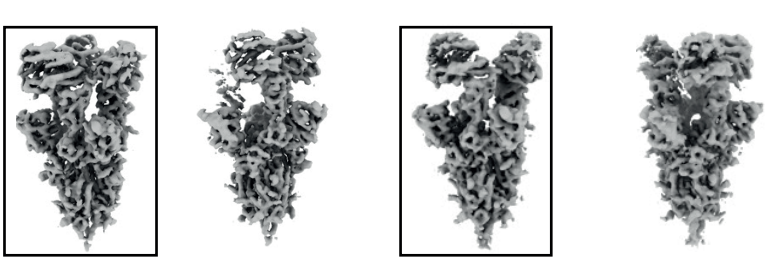

Class 1 | Class 2 | Class 3 | Class 4

38 693 particles
18.5%

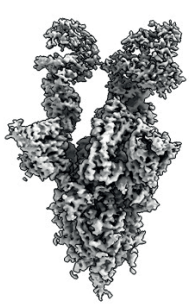

RBD 2-up-mACE2
3.03 Å (C1)

80 674 particles
38.6%

RBD 3-up-mACE2
2.89 Å (C1)

Focussed refinement

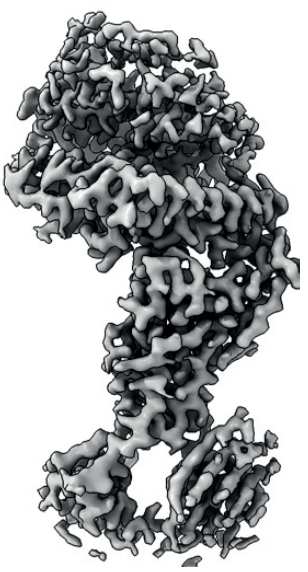

2.96 Å (C1)

**Figure S5**

mACE2 + Omicron BA.4/5

7 989 movies, 0.83 Å/pixel

Cryosparc v3.3.1

Patch motion correction
Patch CTF
Template picker

2 033 320 particles

2 x rounds
2D classification

640 785 particles

Ab-initio reconstruction
Heterogenous refinement

RBD 3-up-mACE2

257 855 particles, 40.2%

Class 1

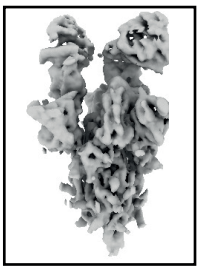

Class 2

Class 3

349 815 particles, 54.6%
Heterogenous refinement

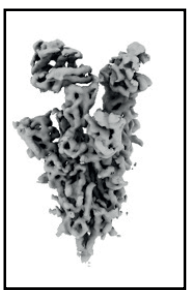

Class 1

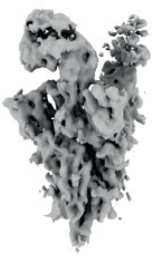

Class 2

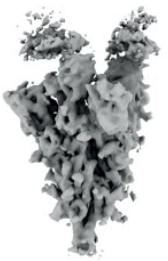

Class 3

Class 4

Class 5

103 496 particles
29.6%

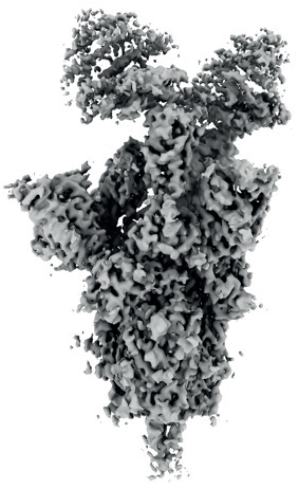

RBD 2-up-mACE2
2.90 Å (C1)

Focussed refinement

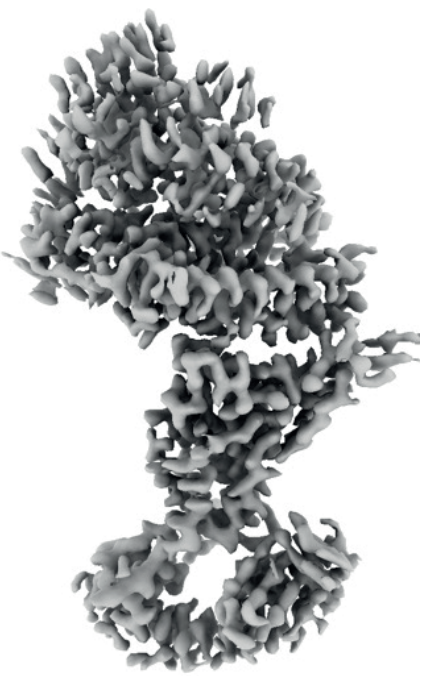

3.3 Å (C1)

**Figure S6**

hACE2 +
Omicron BA.4/5

7 215 movies / 0.83 Å/pix

Cryosparc v3.3.1

Patch motion correction
Patch CTF
Template picker

2 493 631 particles

3 x rounds
2D classification

837 875 particles

Ab-initio reconstruction
Heterogenous refinement


Class 1

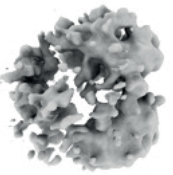
Class 2

777 279 particles
Heterogenous refinement

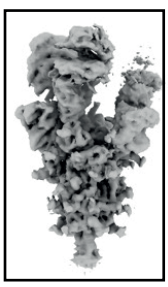
Class 1


Class 2

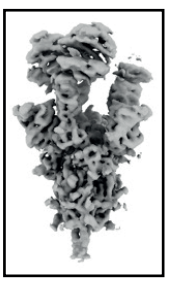
Class 3


Class 4


Class 5


Class 6


Class 7

359 486 particles
Heterogenous refinement

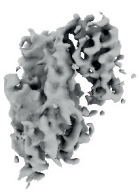
Class 1

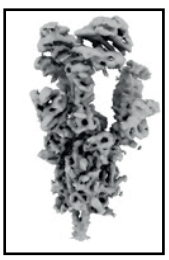
Class 2

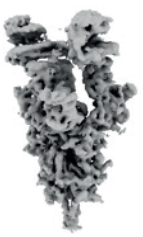
Class 3


Class 4


Class 5

94 718 particles

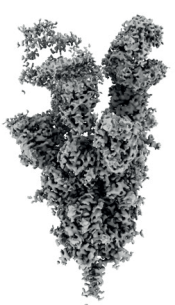
RBD 3-up-mACE2

2.79 Å (C1)

Focussed refinement

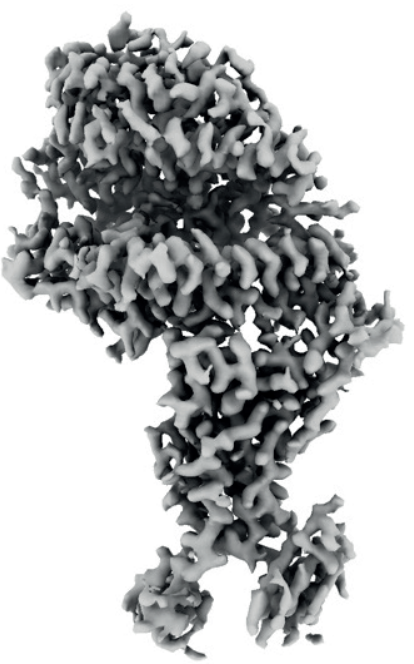
2.92 Å (C1)

**Figure S7**

a

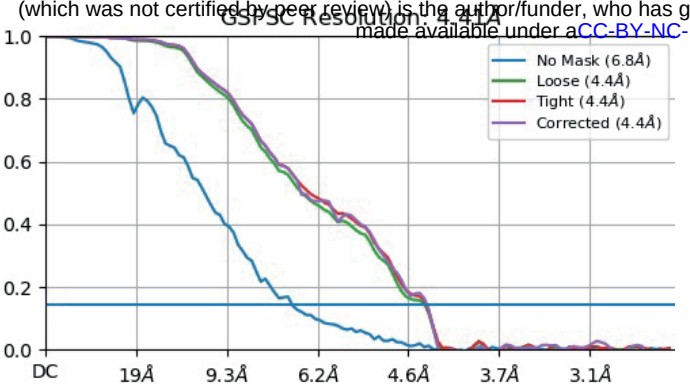


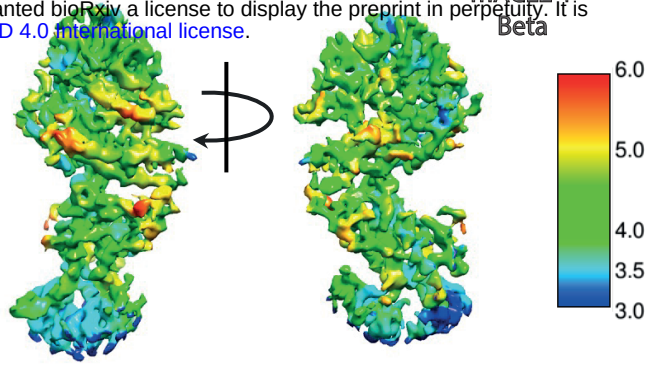


b

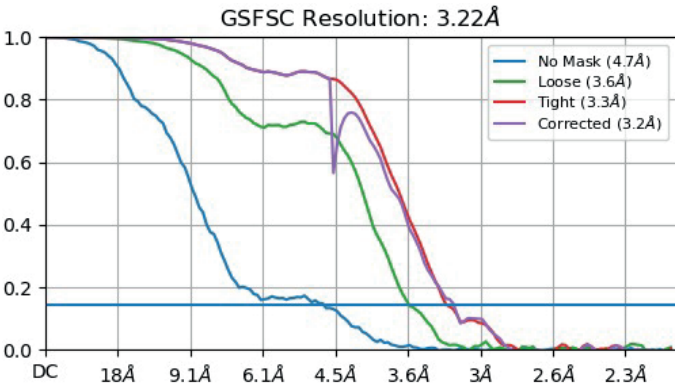


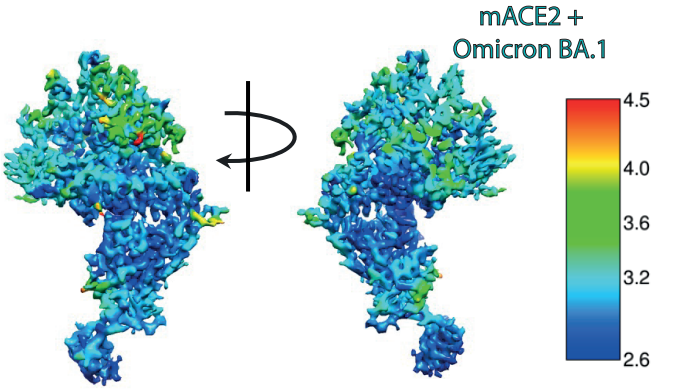


c

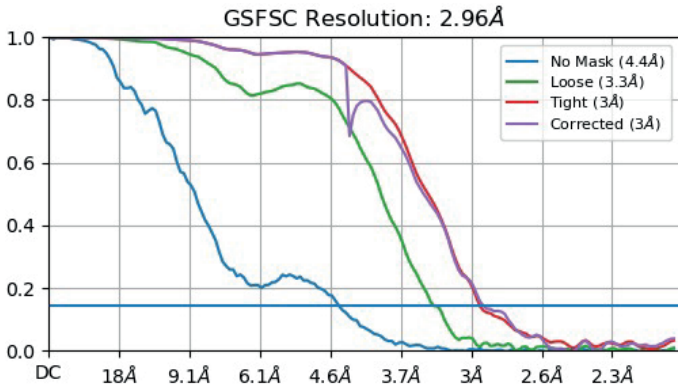


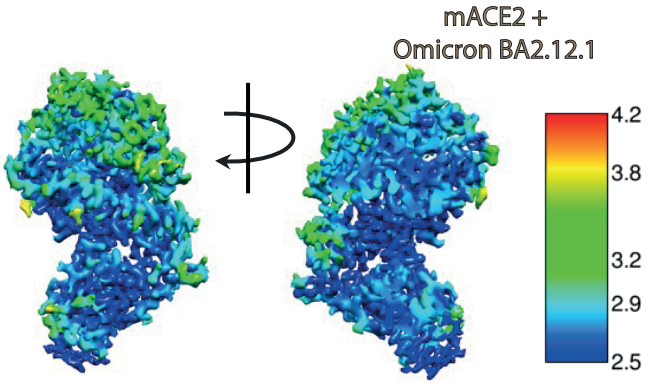


d

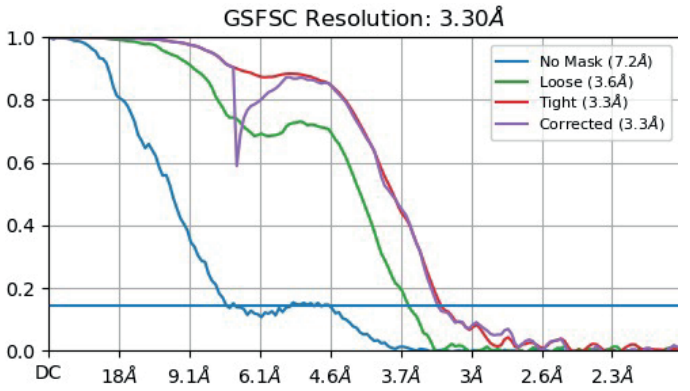


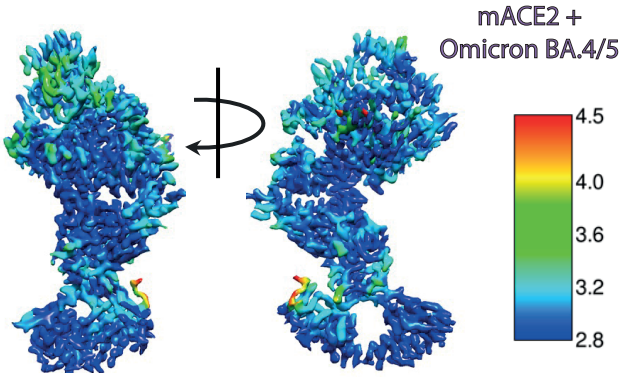


e

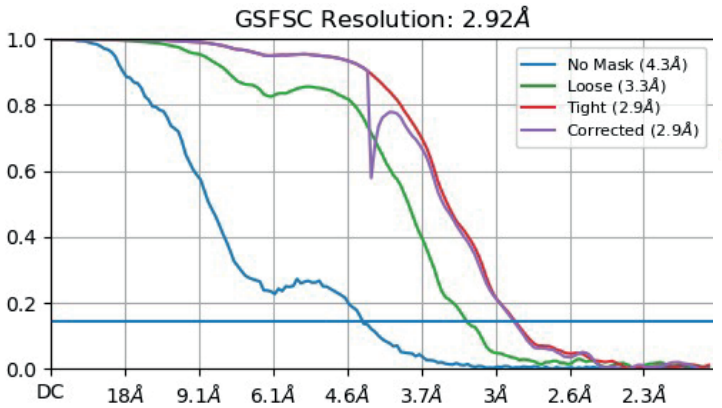


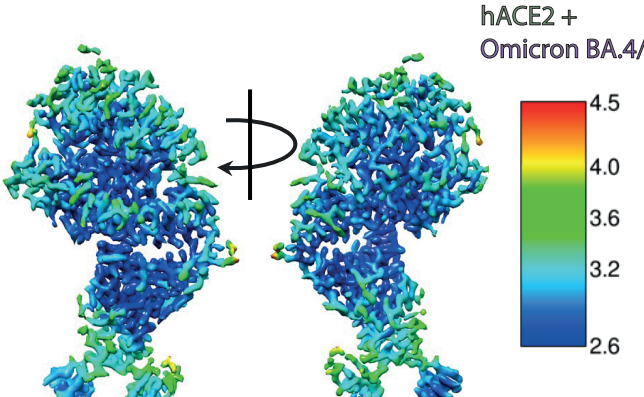


**Figure S8**

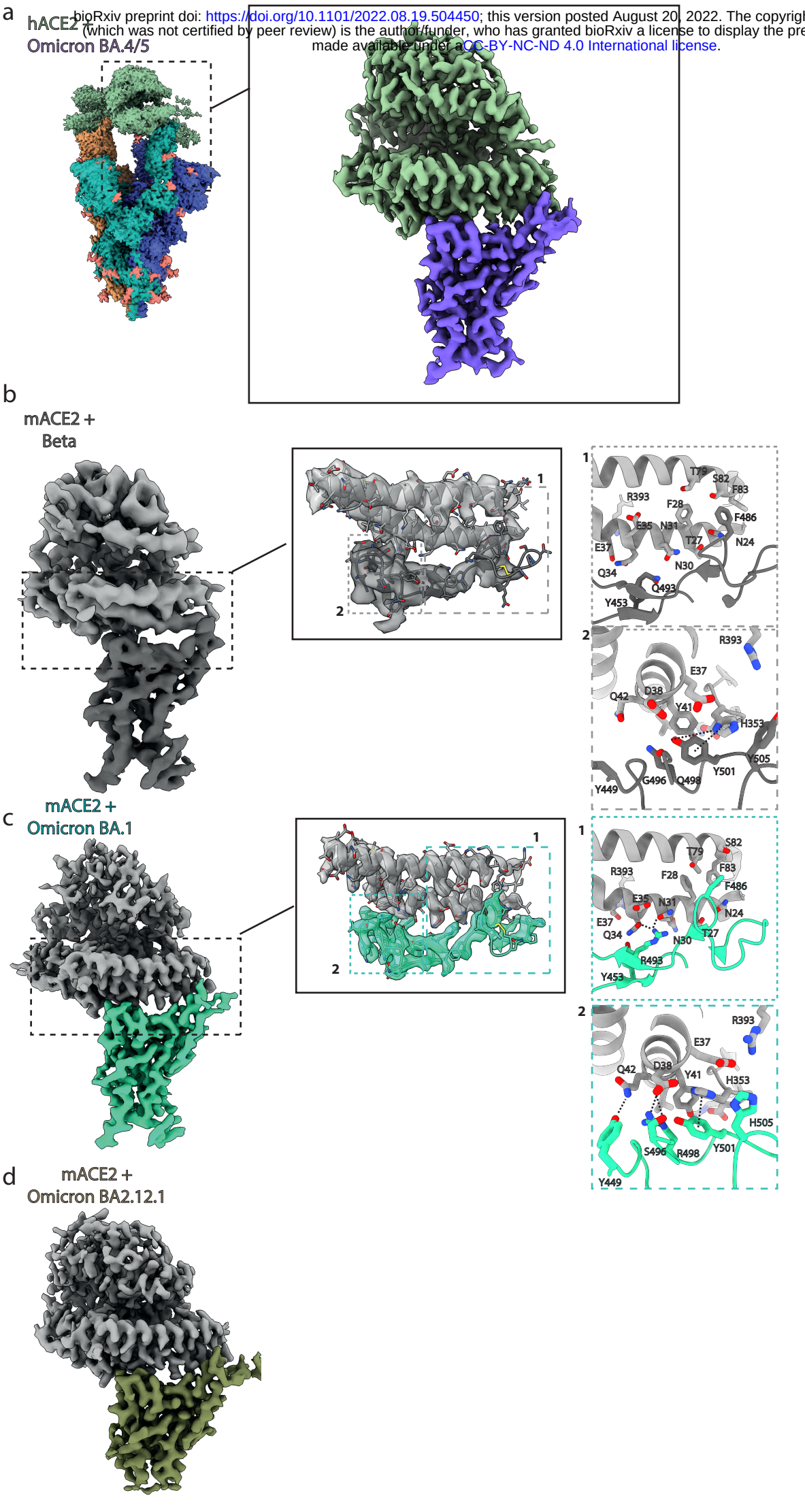


**Figure S9**

## SUPPLEMENTARY FIGURE LEGENDS

**Supplementary information, Fig. S1**: BLI binding assays of mACE2 and hACE2 to various variants and variants of concern. **a** BLI binding assays of captured dimeric mouse or human ACE2 versus various concentrations of BA.2. Data curves are colored by concentration and the black line indicates the 1:1 fit of the data. **b** BLI binding curves of ACE2 at one concentration of 75 nM against a panel of variants of concerns and single mutants. N501Y and E484K mutations together are required for high affinity binding to mACE2 on a prototypic wild-type background.

**Supplementary information, Fig. S2**: Overview of the domain architecture of selected variants of concern. Mutations are shown as red lines and labelled for each variant. Specific domains are highlighted: signal peptide (SP), N- terminal domain (NTD), receptor binding domain (RBD), S1 and S2 domain.

**Supplementary information, Fig. S3**: Cryo-EM processing of the mACE2/Beta complex

**Supplementary information, Fig. S4**: Cryo-EM processing of the mACE2/BA.1 complex

**Supplementary information, Fig. S5**: Cryo-EM processing of the mACE2/BA.2.12.1 complex

**Supplementary information, Fig. S6**: Cryo-EM processing of the mACE2/BA.4/5 complex

**Supplementary information, Fig. S7**: Cryo-EM processing of the hACE2/BA.4/5 complex

**Supplementary information, Fig. S8**: FSC curves indicating resolutions at (FSC 0.143) and final focused refined maps colored by local resolution.

**Supplementary information, Fig. S9**: Additional views of ACE2-Spike variant of concern complexes. **a** Cryo-EM density of the full hACE2/BA.4/5 complexes with the inset showing the focused refinement of the RBD-ACE2 interface. **b** Focused refinement of the RBD-ACE2 interface of the mACE2/Beta complex showing the cryo-EM density. Inset shows the zoomed in view of the binding interface. Further zoomed in views of specific interaction sites of patch 1 and patch 2. **c** Focused refinement of the RBD-ACE2 interface of the mACE2/BA.1 complex showing the cryo-EM density. Inset shows the zoomed in view of the binding interface. Further zoomed in views of specific interaction sites of patch 1 and patch 2. **d** Focused refinement of the RBD-ACE2 interface of the mACE2/BA.2.12.1 complex showing the cryo-EM density.